AMERICAN
METEOROLOGICAL
SOCIETY

Journal of Physical Oceanography

EARLY ONLINE RELEASE

This is a preliminary PDF of the author-produced manuscript that has been peer-reviewed and accepted for publication. Since it is being posted so soon after acceptance, it has not yet been copyedited, formatted, or processed by AMS Publications. This preliminary version of the manuscript may be downloaded, distributed, and cited, but please be aware that there will be visual differences and possibly some content differences between this version and the final published version.

The DOI for this manuscript is doi: 10.1175/2011JPO4573.1

The final published version of this manuscript will replace the preliminary version at the above DOI once it is available.

© 2011 American Meteorological Society

Generated using version 3.0 of the official AMS LaTeX template

Temporal Variability of Diapycnal Mixing in Shag Rocks Passage

Gillian M. Damerell * and Karen J. Heywood

School of Environmental Sciences, University of East Anglia, Norwich, United Kingdom

David P. Stevens

School of Mathematics, University of East Anglia, Norwich, United Kingdom

Alberto C. Naveira Garabato

School of Ocean and Earth Science, National Oceanography Centre, Southampton, United Kingdom

PRELIMINARY ACCEPTED VERSION

Submitted to the Journal of Physical Oceanography, 9 Sept 2010

Revisions submitted 11 March 2011

2nd revisions submitted 14 July 2011

3rd revisions submitted 13 Sept 2011

* *Corresponding author address:* Gillian Damerell, School of Environmental Sciences, University of East Anglia, Norwich, NR4 7TJ, United Kingdom.

E-mail: g.damerell@uea.ac.uk

ABSTRACT

Diapycnal mixing rates in the oceans have been shown to have a great deal of spatial variability, but the temporal variability has been little studied. Here we present results from a method developed to calculate diapycnal diffusivity from moored Acoustic Doppler Current Profiler (ADCP) velocity shear profiles. An 18-month time series of diffusivity is presented from data taken by a LongRanger ADCP moored at 2400 m depth, 600 m above the sea floor, in Shag Rocks Passage, a deep passage in the North Scotia Ridge (Southern Ocean). The Polar Front is constrained to pass through this passage, and the strong currents and complex topography are expected to result in enhanced mixing. The spatial distribution of diffusivity in Shag Rocks Passage deduced from lowered ADCP shear is consistent with published values for similar regions, with diffusivity possibly as large as 90×10^{-4} m^2 s^{-1} near the sea floor, decreasing to the expected background level of $\sim 0.1 \times 10^{-4}$ m^2 s^{-1} in areas away from topography. The moored ADCP profiles spanned a depth range of 2400 to 1800 m; thus the moored time series was obtained from a region of moderately enhanced diffusivity.

The diffusivity time series has a median of 3.3×10^{-4} m^2 s^{-1} and a range of 0.5×10^{-4} m^2 s^{-1} to 57×10^{-4} m^2 s^{-1}. There is no significant signal at annual or semiannual periods, but there is evidence of signals at periods of approximately fourteen days (likely due to the spring-neaps tidal cycle), and at periods of 3.8 and 2.6 days most likely due to topographically-trapped waves propagating around the local seamount. Using the observed stratification and an axisymmetric seamount, of similar dimensions to the one west of the mooring, in a model of baroclinic topographically-trapped waves, produces periods of 3.8 and 2.6 days, in agreement with the signals observed. The diffusivity is anti-correlated

with the rotary coefficient (indicating that stronger mixing occurs during times of upward energy propagation), which suggests that mixing occurs due to the breaking of internal waves generated at topography.

1. Introduction

Diapycnal mixing is considered to be an important component of the three-dimensional ocean circulation (Wunsch and Ferrari 2004). A global average diapycnal diffusivity κ_z of approximately 10^{-4} m^2 s^{-1} is required to maintain the abyssal stratification (Munk and Wunsch 1998). Measurements in the ocean interior, away from boundaries and complex topography, have typically found κ_z of order 0.1×10^{-4} m^2 s^{-1} (Toole et al. 1994; Ledwell et al. 1998; Kunze et al. 2006), whereas in areas with strong currents and complex topography diffusivities can be several orders of magnitude larger (Polzin et al. 1997; Mauritzen et al. 2002; Naveira Garabato et al. 2004; Sloyan 2005). However, most existing measurements or estimates of diffusivity are either snapshots at a single time, or a single integrated value over months or years. The few time series available, such as those discussed by Inall et al. (2000); Rippeth et al. (2002); Palmer et al. (2008); Moum and Nash (2009); Shroyer et al. (2010) are from shallow shelf seas or tidal channels, and cover only a few days or weeks, with the longest (Moum and Nash 2009) spanning a period of four months.

Here we present a method which could, if applied widely, begin to address the question of whether single estimates in the deep ocean can be considered representative of long term values. We derive an 18-month time series of the rate of dissipation of turbulent kinetic energy (ϵ) and κ_z, and discuss some possible mechanisms for the temporal variability seen in these series.

The Scotia Sea, an area of complex topography on the eastern side of Drake Passage (Fig. 1a), has been the focus of a number of studies considering mixing rates (Heywood et al. 2002; Naveira Garabato et al. 2003, 2004). Here, the Subantarctic Front and Polar Front veer northward over the $\sim$ 2000 km long North Scotia Ridge, where the shallow (200-2000 m) topography presents an obstacle to the circumpolar flow of deep waters. The Polar Front is constrained to cross the ridge through Shag Rocks Passage, a 180 km-wide, 3200 m deep fracture zone between 49.6°W and 47.1°W (Moore et al. 1997; Arhan et al. 2002).

As part of the North Scotia Ridge Overflow Project (Smith et al. 2010), CTD (Conductivity-Temperature-Depth) and LADCP (Lowered Acoustic Doppler Current Profiler) profiles were collected between 23 April and 5 May 2003 along the length of the North Scotia Ridge (Fig. 1). Six moorings were placed in Shag Rocks Passage between April 2003 and November 2004 (Walkden et al. 2008), one of which (mooring Shag 2b, water depth 3000 m) included an upward-looking LongRanger ADCP 600 m above bottom (mab) (Table 1 and Fig. 1). The ADCP recorded velocity in 40 bins with a thickness of 16 m, thus observing a total depth of 640 m.

We calculate an 18-month κ_z time series using the method previously used in the Scotia Sea by Naveira Garabato et al. (2004), (originally developed by Gregg and Kunze 1991, with further modifications following Polzin et al. 2002 and Gregg et al. 2003), wherein κ_z can be estimated from profiles of temperature, salinity and current velocity. This relies on the premise that the nonlinear interactions of internal waves initiate an energy cascade to smaller scales, resulting in turbulent dissipation (McComas and Muller 1981; Henyey et al. 1986) from which κ_z can be inferred (Osborn 1980). This method can therefore only assess mixing due to internal wave breaking (and not that due to other non-internal wave processes). This is a valid assumption for this region, as the instruments are not in a region where waters are cascading over a sill, are 600 m off the sea floor so should be away from bottom boundary layers which might be dominated by bottom friction, and are observing water deep enough (>1800 m) that direct wind-driven mixing, such as occurs in the surface mixed layer, is unlikely to occur.

Possible mechanisms for internal wave generation include:

i. Wind forcing can generate near-inertial motions, and, although the large inertial oscillations seen in near-surface waters decrease in amplitude rapidly with depth below the mixed layer (Pollard 1970; Pollard and Millard 1970), they do penetrate somewhat into the ocean interior as internal waves (D'Asaro 1984; Alford 2001, 2003a,b). These could then interact further with the local topography, much of which, along the North Scotia Ridge, is only a few hundred meters deep.

ii. In stratified waters, the interaction of barotropic tidal currents with variable bottom topography can result in the generation of internal tides (Heywood et al. 2007). As discussed by Garrett and St Laurent (2002); St Laurent and Garrett (2002); Garrett and Kunze (2007), most of the energy flux is associated with low modes that propagate away from the generation region, but intense beams of internal tidal energy are generated by certain 'critical' slopes, and lead to local mixing.

iii. In principle, any movement of water over rough topography may generate internal waves (Bell 1975; Baines 1982), which can then initiate an energy cascade to smaller scales and cause turbulent dissipation (McComas and Muller 1981; Henyey et al. 1986).

As well as internal tides, this can be through the generation of lee waves by geostrophic flows (Nikurashin and Ferrari 2010a,b), particularly in the Southern Ocean where bottom geostrophic flows are much more intense than in most other ocean basins. The complex topography in Shag Rocks Passage (Fig. 1d) includes many features at which lee waves could be generated.

iv. The mean flow can also interact with the internal wave field. For example, Kunze and Sanford (1984) and Kunze (1985) observed intense, focussed beams of downward-propagating near-inertial waves at the base of regions of upper ocean negative vorticity. They determined that a wave-mean flow interaction model which predicts trapping and amplification of near-inertial waves in regions of negative vorticity best explained their observations.

The generation from, and interaction with, geostrophic flows may also lead to another indirect link between internal waves and wind forcing, as increased wind speeds can lead to intensified currents, or result in increased eddy activity which transmits momentum downwards through the water column (Bryden 1979; Olbers 1998).

The organisation of this paper is as follows: section 2 begins with a description of the method and uses this to produce a section of κ_z along the North Scotia Ridge, thus setting the spatial context for the moored time series. Section 3 discusses the modifications to the method for use with mooring data and the time series thus obtained. In section 4, spectral analysis is used to identify significant periodicities, and potential sources of temporal variability in κ_z are identified. Section 5 presents the conclusions.

2. Spatial Variability of Diffusivity in Shag Rocks Passage

First, we recap the methodology used by several authors (e.g., Polzin et al. 1995, 2002; Naveira Garabato et al. 2004; Kunze et al. 2006) to estimate ϵ and κ_z from LADCP data. Estimates of κ_z are inferred from velocity shear estimates using a model that assumes a statistical balance between turbulent production, buoyancy flux, and dissipation (Osborn 1980). In common with previous LADCP analyses, we assume that subinertial shear is small compared with that in the internal wave field. The dissipation rate and diapycnal diffusivity are related by $\kappa_z = \Gamma\epsilon/N^2$ where Γ is the mixing efficiency (generally assumed to be 0.2) and N is the buoyancy frequency. The turbulent dissipation rate can be found from:

$$\epsilon = \epsilon_0 \times \frac{f}{f_0}\frac{N^2}{N_0^2}\frac{\cosh^{-1}(N/f)}{\cosh^{-1}(N_0/f_0)}\frac{\langle V_z^2\rangle^2}{\left\langle V_{z-GM}^2\right\rangle^2}\,h_1(R_\omega) \tag{1}$$

(Gregg and Kunze 1991; Polzin et al. 1995, 2002; Gregg et al. 2003). Here $\epsilon_0 = 7.8\times10^{-10}$ W kg^{-1} is the turbulent dissipation rate of the background internal wave field in stratification defined by a buoyancy frequency $N_0 = 5.24\times10^{-3}$ rad s^{-1} at a latitude of 30°, as predicted for the Garrett and Munk (GM) model (Garrett and Munk 1975). f and f_0 are the inertial frequencies at the latitude of observation and at 30° respectively ($f_0 = 7.3\times10^{-5}$ s^{-1} and $f = 1.2\times10^{-4}$ s^{-1}). The latitudinal dependence of the energy cascade to smaller scales is discussed by Gregg et al. (2003). $\langle V_z^2\rangle$ is the variance of the LADCP vertical shear, normalised by N, and $\left\langle V_{z-GM}^2\right\rangle$ is the same variable, as predicted by the GM model. $h_1(R_\omega)$ is a function of the frequency content of the internal wave field (Polzin et al. 1995) estimated from the shear-to-strain ratio R_ω, discussed below.

To derive $\langle V_z^2 \rangle$, each LADCP shear profile is divided into overlapping 320 m segments spaced at 100 m intervals, and normalized by the average buoyancy frequency $\overline{N}$ for that segment. The normalised shear in each segment is Fourier-transformed (64 points) to compute the vertical wavenumber power spectral density. This spectrum is corrected to account for the smoothing in the velocity profiles at high vertical wavenumbers, caused by the spatial averaging inherent in LADCP measurement and data processing (Polzin et al. 2002). Specifically, the corrections described by Polzin et al. (2002) for the finite acoustic transmission and reception intervals, first-differencing of the resulting single-ping velocity profiles, interpolation of the first-differenced profiles onto a regular depth grid, and instrument tilt are applied. $\langle V_z^2 \rangle$ is calculated by integrating the corrected power spectral density between the maximum vertical wavelength of 300 m and a minimum vertical wavelength of 90 m, chosen to minimize the contamination by instrument noise that can occur at higher wavenumbers. This minimum vertical wavelength threshold is selected heuristically by examination of the shear spectra, and the resulting ϵ and κ_z are insensitive to the exact value. $\left\langle V_{z-GM}^2 \right\rangle$ is integrated over the same wavelength range as $\langle V_z^2 \rangle$.

The shear/strain variance ratio R_ω is a measure of the internal wave field's frequency content (Kunze et al. 1990) and is used to parameterize the turbulent dissipation rate in equation (1). R_ω is found from

$$R_\omega = \frac{\langle V_z^2 \rangle}{\langle \xi_z^2 \rangle} = 3 \times \frac{\langle V_z^2 \rangle}{\left\langle V_{z-GM}^2 \right\rangle} \frac{\left\langle \xi_{z-GM}^2 \right\rangle}{\langle \xi_z^2 \rangle}. \tag{2}$$

$\langle \xi_z^2 \rangle$ is the variance of strain, the vertical gradient of the vertical displacement of isopycnals induced by internal waves. $\left\langle \xi_{z-GM}^2 \right\rangle$ is the same variable, as predicted by the GM model, and integrated over the same wavelength range as $\langle \xi_z^2 \rangle$. The factor of three arises because

$\langle V^2_{z-GM} \rangle / \langle \xi^2_{z-GM} \rangle = 3$. Strain is estimated from CTD density profiles using a scale separation assumption (Polzin et al. 1995) and $\langle \xi_z^2 \rangle$ (and R_ω) are calculated in 320 m segments identical to the $\langle V_z^2 \rangle$ bins. R_ω is then averaged horizontally over all stations to give a profile which varies with depth, but does not vary from station to station. $h_1(R_\omega)$ is calculated (Polzin et al. 1995) for each depth as

$$h_1 = \frac{3(R_\omega + 1)}{2\sqrt{2} R_\omega \sqrt{R_\omega - 1}}. \tag{3}$$

The average of R_ω throughout Shag Rocks Passage is 6.0, corresponding to $h_1(R_\omega) = 0.56$. At the depths observed by the mooring, the average R_ω is 7.6, giving $h_1(R_\omega) = 0.47$, and it is this value which is used to parameterize diffusivities calculated from the mooring data, as discussed below.

The κ_z section across Shag Rocks Passage produced from the CTD/LADCP profiles (Fig. 2) shows greatly enhanced κ_z at depth and over complex topography ($\sim 90 \times 10^{-4}$ m^2 s^{-1}), decreasing to a background level of $< 0.1 \times 10^{-4}$ m^2 s^{-1} (consistent with the findings of Toole et al. 1994; Ledwell et al. 1998; Kunze et al. 2006) in areas well away from the sea floor, and at depths of no more than 1000 m. Similarly ϵ varies between $\sim (0.02 - 23) \times 10^{-9}$ W kg^{-1}, and has a comparable spatial pattern (not shown). Both κ_z and ϵ are smoothed horizontally using a 5-station running mean. This section is comparable to published sections elsewhere, particularly those in and around the Scotia Sea (Naveira Garabato et al. 2004; Sloyan 2005). Sloyan's meridional section across the Scotia Sea (her Fig. 3a) is calculated using CTD strain variance techniques, and shows $\kappa_z \sim (10 - 100) \times 10^{-4}$ m^2 s^{-1} near the sea floor, decreasing to $\sim 0.1 \times 10^{-4}$ m^2 s^{-1} or less away from rough topography, consistent with what is observed here.

The section of Naveira Garabato et al. (2004) shows $\kappa_z \sim 100 \times 10^{-4}$ m^2 s^{-1} near the sea floor, with a maximum of nearly 1000×10^{-4} m^2 s^{-1} at the sea floor of Drake Passage and in a deep gap (Orkney Passage) in the South Scotia Ridge (their Fig. 2). Fairly low values of $\sim (0.4 - 4) \times 10^{-4}$ m^2 s^{-1} were observed over the Falkland Plateau, geographically the closest region to the North Scotia Ridge. The much smoother topography of the Falkland Plateau compared with Shag Rocks Passage explains these lower values. The most similar region, in terms of roughness and depth of topography, is the South Scotia Ridge, which shows correspondingly similar results, including enhanced mixing over shallow ($<$ 1500 m depth) topography to the west of the South Orkney Islands, analogous to that seen in Fig. 2 to the west of Shag Rocks Passage. The considerably greater κ_z found by Naveira Garabato et al. in Orkney Passage (nearly 1000×10^{-4} m^2 s^{-1}) than seen anywhere in Shag Rocks Passage may be due to the stronger currents at the sea bed there (velocities approaching 50 cm s^{-1} (Naveira Garabato et al. 2002) as opposed to $\sim$ 20 cm s^{-1} in Shag Rocks Passage). Naveira Garabato et al. (2004) found a sharp reduction in κ_z to values only slightly above 0.1×10^{-4} m^2 s^{-1} in the uppermost 300-400 m of their section in Drake Passage, Orkney Passage and the Scotia Sea. A similar pattern is seen in Fig. 2 between approximately $44 - 49°$W. This region has comparable depths and roughness to the Drake Passage, Orkney Passage and Scotia Sea sections of Naveira Garabato et al. (2004), which have comparable κ_z patterns.

Kunze et al. (2006) raised doubts about the applicability of the shear parameterization in very low abyssal stratifications (their Fig. 3). They argue that noise in LADCP measurements prevents measurement of the shear in areas with $N < 4.5 \times 10^{-4}$ rad s^{-1}, casting doubt on the very high diffusivities at the sea floor of Naveira Garabato et al. (2004). Polzin and Lvov (in press) argue that what has previously been considered noise may in fact be a slow mode consisting of, at lowest order, the steady geostrophic balance. Higher order contributions are time dependence, nonlinearity and the effects of a variable rate of planetary rotation (f). In the section presented here, $N > 4.5 \times 10^{-4}$ rad s^{-1}, except in a very small area below 2700 m, east of the central seamount in Shag Rocks Passage. Moreover, we obtain similar values (not shown) from a strain-only calculation of κ_z independent of the LADCP shear, as used by Mauritzen et al. (2002) and Sloyan (2005). This strain-based calculation of κ_z gives a range of $\sim (0.05 - 100) \times 10^{-4}$ m^2 s^{-1} and a similar spatial pattern to κ_z calculated using LADCP shear. The shear parameterization should therefore be applicable to the moored ADCP time series.

The rotary coefficient of the vertical shear is the ratio of the clockwise and counter-clockwise components of the shear variance, and is a proxy for the ratio of upward to downward energy propagation. It is calculated following Gonella (1972) for the stations in Shag Rocks Passage deeper than 2000 m and lying to the east of the central seamount (Fig. 3). Above $\sim$ 1500 m the propagation is mostly downward, and most likely wind-driven (Alford 2003a). Below $\sim$ 1500 m the propagation is mostly upward, likely due to internal waves generated at the topography (Baines 1973, 1982; Thorpe 1992).

3. Temporal Variability of Diffusivity in Shag Rocks Passage

a. Methodology

The ADCP at mooring Shag2b produced time series of velocity profiles at 2-hour intervals. The method adopted here to calculate κ_z for the time series is essentially the same as described in Section 2 for the LADCP data, repeated for each time interval. There are some modifications to the calculations.

i. Depth Segment and Fourier transform

The shears are treated as one 640 m segment centered at 2100 m depth. After quality control (which consisted of the rejection of points where less than 50% of the measurements had four-beam solutions), generally around 400-500 m remained for use in the Fourier transform, and occasionally as little as 300 m. κ_z is insensitive to the chosen percentage for quality control; using either 25% or 75% as the rejection threshold makes a difference of around 4% to the calculated values, which is small compared with other uncertainties. Since the calculation requires depth bins of at least 320 m of good data, the data were not divided into depth segments in order to retain enough information to calculate the spectral densities. The ADCPs on moorings Shag1b and Shag3b (Table 1 and Fig. 1) recorded velocities in 23 bins of 8 m thickness. After quality control, insufficient depth range remained to resolve wavelengths of 90 m or more, so these could not be used to calculate κ_z.

Each velocity measurement of the ADCP on mooring Shag2b is based on 31 pings, corresponding to an accuracy of approximately 0.6 cm s^{-1}. The LADCP measurements are based on an average of ∼120 pings, giving an accuracy of approximately 0.3 cm s^{-1}. In the stratification observed here (N typically $\sim 8-9 \times 10^{-4}$ s^{-1} in the CTD stations at the depths ensonified by the moored ADCP), typical internal wave speeds are $\sim 1-5$ cm s^{-1} (Thorpe 2005), considerably greater than the accuracy of either instrument.

ii. Buoyancy Frequency

Time series of temperature and salinity were not measured in the volume of water above the mooring in which the currents are sampled by the ADCP. However, a SeaBird Electronics temperature sensor (SBE-39) was mounted on the ADCP, which has a comparable accuracy (±0.002°C) to the ship's CTD (SBE-3*plus*, accuracy ±0.001°C). Each rotary current meter (Table 1) recorded temperature with an accuracy of ±0.05°C. All moored temperature sensors agreed with CTD casts at the beginning and end of the mooring deployment. Here we discuss how best to use these time series to provide time series of temperature and salinity (and hence buoyancy frequency) appropriate to the water column monitored by the ADCP.

13 full depth CTD stations were occupied in Shag Rocks Passage during the deployment cruise, and four during the recovery cruise, that can be used to infer relationships between temperatures at different depths (Fig. 4). The four temperature time series from mooring Shag2(a and b) are linearly related, as are the CTD temperatures at the same depths as the moored temperature sensors. Therefore we fitted the CTD temperature gradient between 1800 and 2400 m, (the depth range observed by the

moored ADCP), to the temperature at 2400 m. Fig. 4(b) illustrates the cubic fit which was found to best reproduce the observed temperature profile. The CTD temperature profiles (Fig. 4a) fall into two groups: a warmer group and a colder group, which lie north and south of the Polar Front respectively. Stations with a higher temperature at 2400 m have a lower temperature gradient, and vice versa (Fig. 4b). The spread in temperatures is thus less at 1800 m depth than at 2400 m. The cubic fit to the CTD stations was used, in conjunction with the temperature at 2400 m recorded by the ADCP, to generate temperature gradients, and thus temperatures, between 1800 and 2400 m for the entire time series.

Similarly, a cubic fit to the CTD T - S relationship (in-situ temperature and salinity respectively) is used to infer salinities between 1800 - 2400 m (Fig. 4). From the temperatures and salinities a time series of buoyancy frequency is deduced. The parameter that has the greatest impact on the calculated κ_z is the temperature gradient, which varies by more than a factor of ten during the time series. As is apparent in Fig. 4(d), salinity varies by no more than 0.009 g kg^{-1} in the ADCP ensonified volume; the effect of salinity on the variability of κ_z is very small.

iii. Spectral Corrections

The corrections described by Polzin et al. (2002) for the finite acoustic transmission and reception intervals, and first-differencing of the resulting single-ping velocity profiles, are applied exactly as for the LADCP shear spectra. We do not need to apply the correction for interpolation of the first-differenced profiles onto a regular depth grid as no interpolation is performed for a moored instrument.

iv. Smoothing

The finescale parameterization used here assumes a stationary internal wavefield, and the stationarity assumption is more likely to hold over a time scale $> 1/f$ (15 hours) than over 2 hours. In a manner similar to the horizontal smoothing of κ_z and ϵ for the spatial section using a 5-station running mean, here we calculate a running mean over 24 hours for κ_z and ϵ. (The length of the running mean was chosen as a compromise between maintaining temporal resolution and the desire to justify the stationarity assumption.) All values quoted from now, or shown in figures or tables, will be those found after applying the running mean unless stated otherwise.

v. Shear-to-strain ratio parameterization

Since we do not have time series of temperature and salinity in the water mass ensonified by the ADCP, we cannot estimate $\langle \xi_z^2 \rangle$ as described in Section 2, and thus cannot calculate a time series for R_ω. Instead, we use the average value of R_ω from the LADCP section over the ensonified depths, which gives $h_1(R_\omega) = 0.47$.

Some examples of the vertical wavenumber spectra of the shear are shown in Fig. 5, and are comparable to those in the literature (e.g., Fig. 2 of Kunze et al. 2006). Fig. 5 also shows the vertical wavenumber spectrum for shear noise: rms noise levels are about (3.2 cm s^{-1})/nping$^{1/2}$ for a large number of scatterers (Polzin et al. 2002), where nping is the number of pings used for each velocity measurement. Over the interval of integration (90 - 300 m), the spectra are relatively flat, and are clearly distinguishable from the noise spectrum. At higher wavenumbers (wavelengths <90 m) the spectra are dominated by noise, which illustrates the validity of the choice of 90 m as the minumum wavelength over which the spectra are integrated.

b. *Resultant Time Series*

Fig. 6 shows the time series of ADCP velocity, integrated shear variance, temperatures, depth-average buoyancy frequency $\overline{N}$, rotary coefficient and the derived κ_z. The integrated shear variance is $\langle V_z^2 \rangle$ without the normalization by $\overline{N}$, so as to show the shear and buoyancy frequency separately. Included for comparison is the 6-hourly wind speed from the ECMWF reanalysis dataset ERA-Interim, (ECMWF cited 2009), at the nearest grid point (48°W, 52.5°S) to mooring Shag2b. All the mooring time series show good agreement with the values obtained from the closest CTD/LADCP stations of the deployment and recovery cruises. The time series of ϵ is not shown, as it is so strongly correlated with κ_z ($r = 0.98$) that it does not provide additional information.

κ_z has a mean of 4.1×10^{-4} m^2 s^{-1}, median of 3.3×10^{-4} m^2 s^{-1} and covers a range from 0.5×10^{-4} to 57×10^{-4} m^2 s^{-1}. At the depths ensonified by the moored ADCP, the spatial section (Fig. 2) has κ_z varying from 0.3×10^{-4} to 20×10^{-4} m^2 s^{-1}, with a mean of 3.1×10^{-4} m^2 s^{-1}. The range in the spatial section across Shag Rocks Passage is consistent with the range of the time series, especially given the inherent uncertainty in the method (reported by Polzin et al. (2002) to be around a factor of 3-4).

None of the time series (Fig. 6) display annual or semi-annual signals, such as those seen by Large and Van Loon (1989) in Southern Ocean winds. There is no significant correlation between the local wind speed and any of the mooring records (Fig. 6), or the velocity and temperature of the other moorings in Shag Rocks Passage (Table 1 and Fig. 1). The possible influence of the winds or atmospheric pressure (direct or indirect) was further investigated by searching for correlations between κ_z and the wind speed and atmospheric pressure at sea level, bandpass filtered to near-inertial periods, using the ERA-Interim dataset, (ECMWF cited 2009) in the entire region south of 30°S. Lags of up to 80 days were considered. No significant correlations were found.

Table 2 lists statistics of the time series of integrated shear variance, buoyancy frequency, dissipation rate, rotary coefficient and diffusivity. The agreement is good between the first values of the time series and the LADCP values taken from the nearest station of the deployment cruise and averaged over the same depths observed by the moored ADCP. This station was occupied approximately 7 hours before the start of the mooring record. All (except the rotary coefficient) have rather non-normal distributions, as indicated by their large skewness and excess kurtosis, although the integrated shear variance and buoyancy frequency are much less extreme than ϵ and κ_z. Higher kurtosis indicates that more of the variance is the result of infrequent extreme deviations, as opposed to frequent modestly sized deviations. Averaging over periods of 5 days or more gives a significantly more stable mean. The distribution of κ_z is shown in Fig. 7, and is log-normal, consistent with microstructure turbulence observations (e.g., Gregg et al. 1993).

The time-varying temperature gradient used to calculate the buoyancy frequency affects the calculated κ_z. If we had instead used a constant temperature gradient of that measured at the nearest station of the deployment cruise (averaged over the appropriate depths), the range of κ_z would instead be $(0.3 - 62) \times 10^{-4}$ m^2 s^{-1}, with a median of 3.2×10^{-4} m^2 s^{-1}. Using the fit described above to extrapolate temperature, but replacing the fit for salinity with the average CTD salinity profile (i.e., not varying salinity with time), the range of κ_z

would be $(0.5-54)\times10^{-4}$ m^2 s^{-1}, with a median of 3.2×10^{-4} m^2 s^{-1}. The time series of κ_z calculated using a constant salinity profile is virtually indistinguishable from that calculated using the fitted salinities.

The distribution of the rotary coefficient (Fig. 8) is approximately normal, as indicated by the low skewness and excess kurtosis, and the mean value of -0.11 indicates weak upward energy propagation at these depths (1800 - 2400 m). The LADCP-derived rotary coefficient is only just within one standard deviation of the time series mean, but still lies well within the range of the time series. The rotary coefficient is relatively low at the start of the time series (Fig. 6), i.e., when the LADCP-derived value was obtained.

Comparison of these time series shows the separate effects of shear and buoyancy frequency in the derivation of κ_z: peaks in integrated shear variance appear as peaks in κ_z (with a particularly strong peak in October 2004), whereas peaks in buoyancy frequency appear as troughs in κ_z. Correlations between the time series (Table 3) show that integrated shear variance and κ_z are strongly correlated, with $r = 0.89$, whereas buoyancy frequency and κ_z are much more weakly anti-correlated ($r = -0.31$), indicating that variations in κ_z are dominated by variations in shear.

The moderately strong correlation between temperature and buoyancy frequency ($r = 0.47$) is apparent in Fig. 6, although due to the nature of the fit used (Fig. 4) strong peaks in temperature appear as troughs in buoyancy frequency rather than peaks. The mooring lies very close to the Polar Front (Fig. 2), so we hypothesize that the front may have moved over the mooring, possibly multiple times during the 18 month deployment. The CTD stations confirm that the front moved over the mooring at least once: the deployment cruise CTD closest to mooring Shag2b is the coldest of the profiles (Fig. 4a) and lies to the south of the Polar Front, whereas the recovery cruise CTD taken at the same location is within the warmer group to the north of the Polar Front. Smith et al. (2010) observed that the front moved $\sim 1^\circ$ (65 km) to the west in 11 days during the deployment cruise. The temperature time series is not correlated with the velocity or shear, and the stratification of the CTD stations north and south of the front is similar (the range in buoyancy frequency is small), so the possible movement of the front during the mooring deployment does not have a strong influence on κ_z.

The weak anti-correlation between κ_z and rotary coefficient ($r = -0.40$) suggests that when the rotary coefficient is low, indicating more upward propagating energy (probably from internal waves generated at the topography), κ_z is high, presumably from more internal wave breaking. Fig. 6 reveals coincident troughs in rotary coefficient and peaks in κ_z.

The effects of mooring knockdown and tilt have been considered. From the ADCP pressure record the maximum knockdown of 180 m occurred during a 2-week period of particularly strong currents in May 2003, but, during the rest of the record, the knockdown rarely exceeded 20 m. Similarly the pitch and roll reach maxima of 3° and 5° respectively during the same period, but otherwise rarely exceed 1°. These are not thought to have a significant effect on the shear or buoyancy frequency, and thus on κ_z, for two reasons. Firstly, the depth, pitch and roll are not correlated with shear, buoyancy frequency or κ_z. Secondly, we considered what size of knockdown or tilt would be necessary to produce the observed ranges of shear and buoyancy frequency in the absence of varying currents and temperatures. The required knockdowns of nearly 700 m to produce the observed range in shear, and over 1500 m to produce the observed range in buoyancy frequency, are both greater than the total height of the mooring, and far exceed the observed knockdown. Buoyancy frequency will not be affected by the tilt, since it is extrapolated from temperature readings at the depth of the ADCP only. The tilt required to produce the observed range in shear is nearly 65°; far greater than the observed range in pitch or roll. We therefore conclude that the variations seen in κ_z are caused by changes in the ocean's tubulent flow and not artefacts of the mooring motion.

4. Spectral Analysis

Using the multi-taper method (Thomson 1982; Percival and Walden 1993), we performed spectral analysis to search for significant periodicities which could be linked to a particular source of variability. Spectra are shown in Fig. 9 for the northward and eastward depth-mean velocities, temperature at 2400 m, ECMWF reanalysis wind speed at the nearest grid point to mooring Shag2b, integrated shear variance (both with and without the smoothing described in section 3.a.iv), buoyancy frequency, and κ_z with the smoothing described in section 3.a.iv. We include the smoothed integrated shear variance for ease of comparison with the smoothed κ_z. Each plot also shows the theoretical red noise spectrum calculated from the lag-1 autocorrelation coefficient for that variable, except for plot (e), the unsmoothed integrated shear variance. Since many oceanographic quantities are approximately red, this was used as a null hypothesis: peaks in the spectra are considered significantly different from a red noise background if they lie above the 95% confidence limit of the red noise spectrum.

The main diurnal (O1 and K1) and semi-diurnal (M2 and S2) tidal frequencies are visible in the velocities (Fig. 9a & b), particularly in the northward velocity. Very small peaks at the local inertial frequency (0.067 cycles/day, period 15.0 hours) are also present. The spectrum of the integrated shear variance calculated without the smoothing described in section 3.a.iv. (Fig. 9e) shows that the integrated shear variance is very energetic at high frequencies. This demonstrates the validity of the assumption stated in section 2 that subinertial shear is small compared with that in the internal wave field. Both the unsmoothed integrated shear variance and unsmoothed κ_z (not shown) are energetic at high frequencies, but do not display a particularly noticable increase in activity at inertial, diurnal or semi-diurnal frequencies. While this might suggest that the inertial and diurnal/semi-diurnal tidal components of the velocities are barotropic rather than baroclinic, Sherman and Pinkel (1991) point out that small scale internal waves (which contribute the most shear) are vertically heaved by other internal waves. This Doppler shifts the encounter frequency as measured by a fixed mooring across frequency space so that the intrinsic frequency of the waves cannot be identified.

The northward (along-stream) velocity shows high spectral energy in a broad band from 10 to 60 days, with a noticeable peak around 14 days, the period of the spring-neaps tidal cycle, whereas the eastward (cross-stream) velocity is most energetic in the band from 2 to 5 days, with a particularly large peak at a period of approximately 4 days. Although the wind speed shows variability at periods between 6 hours and $\sim$6 days, it is not correlated or coherent with the current velocity, so is not a direct driver of that variability. Comparison with other ACC current meter velocities suggests that the topographic constriction in the east-west direction is responsible for the difference, in the energetic frequencies, exhibited by the northward and eastward velocities. Bryden and Heath (1985) examined moored current meter data southeast of New Zealand, and in central Drake Passage. Phillips and Rintoul (2000) examined moored current meter data in the ACC south of Australia. Both studies suggest that, in areas with topographic constrictions, the cross-stream velocity tends to exhibit variability at shorter periods than the along-stream velocity. The spectrum of the temperature time series shows rather different behavior to the velocities, with low variability at high frequencies but a significant peak at periods of $\sim$ 50 - 100 days. This is comparable to the temperature spectra found by Bryden and Heath (1985) and Phillips and Rintoul (2000).

The variability at periods of 10-20 days in the spectra of integrated shear variance and buoyancy frequency, and thus κ_z and rotary coefficient (spectrum not shown, but broadly similar to the spectra of κ_z and integrated shear variance), is most likely due to the spring-neaps tidal cycle, combined with eddy activity, which several authors have reported as important at these periods (Bryden 1979; Sciremammano 1980; Bryden and Heath 1985).

The large peak at a period of 3.8 days seen in the spectra of eastward velocity, integrated shear variance and κ_z is particularly unexpected. Bandpass filtering reveals that the signal is very persistent, appearing throughout the κ_z record, with an average amplitude of approximately 1.5×10^{-4} m^2 s^{-1}. It is not an instrumental fault as the same signal appears in the velocities recorded by the RCMs below the ADCP. It is not directly wind-driven, as the winds are neither correlated nor coherent with κ_z. Moreover, wind-driving would be expected to be apparent over a fairly wide area, and the velocities at moorings Shag1 and Shag3 (Fig. 1(c) and Table 1) do not show a signal at that period. It is not caused by seiching, as the constricted channel is too short in the north-south direction and too wide in the east-west direction to set up such a resonance. In 4 days, water is advected north by an average of 60km, which is more than the north-south length of the constriction. Bandpass filtering the velocities and plotting a progressive vector diagram (not shown) reveals that this east-west oscillation has an amplitude of approximately 5km. This is too great to be caused by mooring motion since the ADCP is only 600 m off the sea floor, and spectra of the mooring's depth, pitch and roll do not reveal a large 3.8-day signal. One remaining possibility is topographically-trapped Rossby waves propagating around the local seamount. The mooring is located on the north-east flank of a seamount (Fig. 1(c) and Fig. 2) with a radius of $\sim$15 km at its base, and a slope of $\sim$55 m/km. LeBlond and Mysak (1978) state that wave-trapping by a cylindrical seamount (i.e., a seamount with vertical sides) is only possible if the radius of the seamount is greater than the barotropic Rossby radius (1300 km in Shag Rocks Passage, so much greater than the radius of this seamount). However, subinertial waves can be trapped by a seamount with sloping sides (Rhines 1969; Brink 1989; Sanson 2010) even if the radius of the seamount is less than the barotropic Rossby radius.

Using the model of Brink (1989) with the stratification observed during the deployment cruise and an idealised, axisymmetric seamount (Fig. 10) of similar height, radius and slope to the one immediately west of the mooring, we find trapped waves with azimuthal wavenumber $n = 1$ and a frequency of 3.0 $\times 10^{-6}$ s^{-1} (period 3.8 days), consistent with the observed primary peak in the κ_z spectrum of 3.8 days. (Model downloaded 6/20/2011 from http://www.whoi.edu/page.do?pid=23361.) At $n = 2$ the model finds a trapped wave with a frequency of 4.5 $\times 10^{-6}$ s^{-1} (period 2.6 days), consistent with the second most prominent peak in the spectrum of κ_z. Although the velocities in Fig. 9(a) and (b) do not have obvious peaks at a period of 2.6 days, these are the spectra of the depth-mean velocities, i.e., the barotropic component. The integrated shear variance (Fig. 9f) has peaks at periods of 3.8 days and 2.6 days, indicating that these are baroclinic motions. Such baroclinic motions can increase the internal wave shear variance and thus κ_z.

5. Conclusions

An 18-month time series of internal wave driven diapycnal diffusivity from Shag Rocks Passage was inferred from fine scale shear using a method modified from that used to calculate κ_z from LADCP shears. The mean κ_z was 4.1×10^{-4} m^2 s^{-1}, consistent with the value obtained from LADCP data of 6.4×10^{-4} m^2 s^{-1} at the depths ensonified by the moored ADCP. κ_z varies by a factor of just over 100, much greater than the factor of 3-4 uncertainty inherent in the method (Polzin et al. 2002), from 0.5×10^{-4} to 57×10^{-4} m^2 s^{-1}. This range is slightly greater than the spatial variability seen in Shag Rocks Passage at the same depths as ensonified by the moored ADCP. The record shows no obvious annual or semiannual cycle, despite being at a high latitude where seasonality is often quite marked. The record displays variability over timescales of 10 to 20 days thought to be driven by eddy activity and the spring-neap tidal cycle, and variability at periods of 3.8 and 2.6 days most likely due to topographically-trapped waves propagating around the local seamount. κ_z is anti-correlated with the rotary coefficient (indicating that stronger mixing occurs during times of upward energy propagation), which suggests that mixing occurs due to the breaking of internal waves generated at topography. We have demonstrated that time series can, to an extent, shed light on the mechanisms causing mixing.

The results presented here are from a single moored ADCP in a rather atypical location, where a strong flow is extremely constrained by the topography. The moorings used were not designed to measure κ_z, but we have demonstrated that the method used to calculate κ_z from CTD/LADCP profiles can be adapted for use with moored instruments. If measuring κ_z were the aim, then in regions with a less stable temperature-salinity relationship, or where a linear temperature gradient is not an appropriate assumption, the moorings would need to include temperature and salinity sensors spanning the depth range ensonified by the moored ADCP. It is also necessary to programme the ADCP to provide both sufficient vertical resolution, and enough depth bins to perform a Fourier transform in the vertical. The vertical sampling frequency must be at least twice the largest wavenumber included in the integration, i.e. the length of the depth bins must be, at most, half the smallest wavelength included. Moreover, finescale parameterizations have not been assessed for depth bins greater than 20m. We would therefore recommend using depth bins of no more than 20-40 m. The decision on what constitutes 'enough' depth bins is rather heuristic, but we would recommend a minimum of 15-20 bins of good data (i.e. after the data quality control cuts, such as that based on the percentage of good beam solutions, have been made).

Time series at other locations will be important in assessing whether diapycnal mixing commonly varies over a similar range, or whether this is simply a feature of this particular location. In the Scotia Sea region, there is considerable atmospheric variability such as storms and seasonal cycles, and in the ocean, variability includes extensive eddy activity, strong currents, and movement of fronts. Shag Rocks Passage has complex topography, with which varying water motions can interact. We postulate that other regions with less atmospheric and oceanic variability, and less complex topography, may experience less temporal variability in κ_z at the depths observed here. We are therefore cautiously optimistic about the validity of 'snapshots' of κ_z, though we would prefer to see further studies of temporal variability over at least a year at a range of locations, especially since local topography (e.g., small seamounts) can provide variability on timescales unrelated to large-scale atmospheric forcing.

Acknowledgments.

The CTD, LADCP and mooring data were acquired as part of the North Scotia Ridge Overflow project, funded by the Natural Environment Research Council grant NER/G/S/2001/00006 through the Antarctic Funding Initiative. A Natural Environment Research Council PhD studentship at UEA supported G.M.D. during the analysis and writing of this report. We thank Gareth Janacek and Adrian Matthews for useful discussions on spectral analysis, and our anonymous reviewers for their insightful comments. The ERA-Interim data were obtained from ECMWF at http://www.ecmwf.int/research/era/do/get/index. The Brink model is made available at http://www.whoi.edu/page.do?pid=23361. Alex Tate kindly provided multibeam bathymetry from the British Antarctic Survey Marine Geophysical Database.

REFERENCES

Alford, M. H., 2001: Internal swell generation: The spatial distribution of energy flux from the wind to mixed layer near-inertial motions. *J. Phys. Oceanogr.*, **31 (8)**, 2359–2368.

Alford, M. H., 2003a: Improved global maps and 54-year history of wind-work on ocean inertial motions. *Geophys. Res. Lett.*, **30 (8)**, 1424.

Alford, M. H., 2003b: Redistribution of energy available for ocean mixing by long-range propagation of internal waves. *Nature*, **423 (6936)**, 159–162.

Arhan, M., A. C. Naveira Garabato, K. J. Heywood, and D. P. Stevens, 2002: The Antarctic Circumpolar Current between the Falkland Islands and South Georgia. *J. Phys. Oceanogr.*, **32 (6)**, 1914–1931.

Baines, P. G., 1973: Generation of internal tides by flat-bump topography. *Deep-Sea Res.*, **20 (2)**, 179–205.

Baines, P. G., 1982: On internal tide generation models. *Deep-Sea Res.*, **29 (3)**, 307–338.

Bell, T. H., 1975: Topographically generated internal waves in open ocean. *J. Geophys. Res.*, **80 (3)**, 320–327.

Brink, K. H., 1989: The effect of stratification on seamount-trapped waves. *Deep-Sea Res.*, **36 (6)**, 825–844.

Bryden, H. L., 1979: Poleward heat-flux and conversion of available potential-energy in Drake Passage. *J. Mar. Res.*, **37 (1)**, 1–22.

Bryden, H. L. and R. A. Heath, 1985: Energetic eddies at the northern edge of the Antarctic Circumpolar Current in the Southwest Pacific. *Progress In Oceanography*, **14 (1-4)**, 65–87.

D'Asaro, E. A., 1984: Wind forced internal waves In the North Pacific and Sargasso Sea. *J. Phys. Oceanogr.*, **14 (4)**, 781–794.

ECMWF, cited 2009: European Centre for Medium-Range Weather Forecasts. ECMWF ERA-Interim re-analysis data. British Atmospheric Data Centre. Available online at http://badc.nerc.ac.uk/data/ecmwf-era-interim/.

Garrett, C. and E. Kunze, 2007: Internal tide generation in the deep ocean. *Annu. Rev. Fluid Mech.*, **39**, 57–87.

Garrett, C. and W. Munk, 1975: Space-time scales of Internal Waves - Progress Report. *J. Geophys. Res.*, **80 (3)**, 291–297.

Garrett, C. and L. St Laurent, 2002: Aspects of deep ocean mixing. *Journal of Oceanography*, **58 (1)**, 11–24.

Gonella, J., 1972: Rotary-component method for analyzing meteorological and oceanographic vector time series. *Deep-Sea Res.*, **19 (12)**, 833–846.

Gregg, M. C. and E. Kunze, 1991: Shear and strain in Santa-Monica Basin. *J. Geophys. Res.*, **96 (C9)**, 16 709–16 719.

Gregg, M. C., T. B. Sanford, and D. P. Winkel, 2003: Reduced mixing from the breaking of internal waves in equatorial waters. *Nature*, **422 (6931)**, 513–515.

Gregg, M. C., H. E. Seim, and D. B. Percival, 1993: Statistics of shear and turbulent dissipation profiles in random internal wave-fields. *J. Phys. Oceanogr.*, **23 (8)**, 1777–1799.

Henyey, F. S., J. Wright, and S. M. Flatte, 1986: Energy and action flow through the internal wave field - an eikonal approach. *J. Geophys. Res.*, **91 (C7)**, 8487–8495.

Heywood, K. J., J. L. Collins, C. W. Hughes, and I. Vassie, 2007: On the detectability of internal tides in Drake Passage. *Deep-Sea Res.*, **54 (11)**, 1972–1984.

Heywood, K. J., A. C. Naveira Garabato, and D. P. Stevens, 2002: High mixing rates in the abyssal Southern Ocean. *Nature*, **415 (6875)**, 1011–1014.

Inall, M. E., T. P. Rippeth, and T. J. Sherwin, 2000: Impact of nonlinear waves on the dissipation of internal tidal energy at a shelf break. *J. Geophys. Res.*, **105 (C4)**, 8687–8705.

Jackett, D. R. and T. J. McDougall, 1997: A neutral density variable for the world's oceans. *J. Phys. Oceanogr.*, **27 (2)**, 237–263.

Kunze, E., 1985: Near-inertial wave-propagation in geostrophic shear. *J. Phys. Oceanogr.*, **15 (5)**, 544–565.

Kunze, E., E. Firing, J. M. Hummon, T. K. Chereskin, and A. M. Thurnherr, 2006: Global abyssal mixing inferred from lowered ADCP shear and CTD strain profiles. *J. Phys. Oceanogr.*, **36 (8)**, 1553–1576.

Kunze, E. and T. B. Sanford, 1984: Observations of near-inertial waves in a front. *J. Phys. Oceanogr.*, **14 (3)**, 566–581.

Kunze, E., A. J. Williams, and M. G. Briscoe, 1990: Observations of shear and vertical stability from a neutrally buoyant float. *J. Geophys. Res.*, **95 (C10)**, 18 127–18 142.

Large, W. G. and H. Van Loon, 1989: Large-scale, low-frequency variability of the 1979 FGGE surface buoy drifts and winds over the southern hemisphere. *J. Phys. Oceanogr.*, **19 (2)**, 216–232.

LeBlond, P. and L. Mysak, 1978: *Waves in the Ocean*. Elsevier.

Ledwell, J. R., A. J. Watson, and C. S. Law, 1998: Mixing of a tracer in the pycnocline. *J. Geophys. Res.*, **103 (C10)**, 21 499–21 529.

Mauritzen, C., K. L. Polzin, M. S. McCartney, R. C. Millard, and D. E. West-Mack, 2002: Evidence in hydrography and density fine structure for enhanced vertical mixing over the Mid-Atlantic Ridge in the western Atlantic. *J. Geophys. Res.*, **107 (C10)**, C103 147.

McComas, C. H. and P. Muller, 1981: The dynamic balance of internal waves. *J. Phys. Oceanogr.*, **11 (7)**, 970–986.

Moore, J. K., M. R. Abbott, and J. G. Richman, 1997: Variability in the location of the Antarctic Polar Front (90 degrees-20 degrees W) from satellite sea surface temperature data. *J. Geophys. Res.*, **102 (C13)**, 27 825–27 833.

Moum, J. N. and J. D. Nash, 2009: Mixing measurements on an equatorial ocean mooring. *J. Atmos. Oceanic Technol.*, **26 (2)**, 317–336.

Munk, W. and C. Wunsch, 1998: Abyssal recipes II: energetics of tidal and wind mixing. *Deep-Sea Res.*, **45 (12)**, 1977–2010.

Naveira Garabato, A. C., E. L. McDonagh, D. P. Stevens, K. J. Heywood, and R. J. Sanders, 2002: On the export of Antarctic Bottom Water from the Weddell Sea. *Deep-Sea Res.*, **49 (21)**, 4715–4742.

Naveira Garabato, A. C., K. L. Polzin, B. A. King, K. J. Heywood, and M. Visbeck, 2004: Widespread intense turbulent mixing in the Southern Ocean. *Science*, **303 (5655)**, 210–213.

Naveira Garabato, A. C., D. P. Stevens, and K. J. Heywood, 2003: Water mass conversion, fluxes, and mixing in the Scotia Sea diagnosed by an inverse model. *J. Phys. Oceanogr.*, **33 (12)**, 2565–2587.

Nikurashin, M. and R. Ferrari, 2010a: Radiation and dissipation of internal waves generated by geostrophic motions impinging on small-scale topography: application to the Southern Ocean. *J. Phys. Oceanogr.*, **40 (9)**, 2025–2042.

Nikurashin, M. and R. Ferrari, 2010b: Radiation and dissipation of internal waves generated by geostrophic motions impinging on small-scale topography: Theory. *J. Phys. Oceanogr.*, **40 (5)**, 1055–1074.

Olbers, D., 1998: Comments on "On the obscurantist physics of 'form drag' in theorizing about the Circumpolar Current". *J. Phys. Oceanogr.*, **28 (8)**, 1647–1654.

Orsi, A. H., T. Whitworth, and W. D. Nowlin, 1995: On the meridional extent and fronts of the Antarctic Circumpolar Current. *Deep-Sea Res.*, **42 (5)**, 641–673.

Osborn, T. R., 1980: Estimates of the local-rate of vertical diffusion from dissipation measurements. *J. Phys. Oceanogr.*, **10 (1)**, 83–89.

Palmer, M. R., T. P. Rippeth, and J. H. Simpson, 2008: An investigation of internal mixing in a seasonally stratified shelf sea. *J. Geophys. Res.*, **113 (C12)**, C12 005.

Percival, D. and A. Walden, 1993: *Spectral Analysis for Physical Applications: Multitaper and Conventional Univariate Techniques*. Cambridge University Press.

Phillips, H. E. and S. R. Rintoul, 2000: Eddy variability and energetics from direct current measurements in the Antarctic Circumpolar Current south of Australia. *J. Phys. Oceanogr.*, **30 (12)**, 3050–3076.

Pollard, R. T., 1970: On generation by winds of inertial waves in ocean. *Deep-Sea Res.*, **17 (4)**, 795–&.

Pollard, R. T. and R. C. Millard, 1970: Comparison between observed and simulated wind-generated inertial oscillations. *Deep-Sea Res.*, **17 (4)**, 813–821.

Polzin, K., E. Kunze, J. Hummon, and E. Firing, 2002: The finescale response of lowered ADCP velocity profiles. *J. Atmos. Oceanic Technol.*, **19 (2)**, 205–224.

Polzin, K. L. and Y. V. Lvov, in press: Towards regional characterizations of the oceanic internal wavefield. *Rev. Geophys.*

Polzin, K. L., J. M. Toole, J. R. Ledwell, and R. W. Schmitt, 1997: Spatial variability of turbulent mixing in the abyssal ocean. *Science*, **276 (5309)**, 93–96.

Polzin, K. L., J. M. Toole, and R. W. Schmitt, 1995: Finescale parameterizations of turbulent dissipation. *J. Phys. Oceanogr.*, **25 (3)**, 306–328.

Rhines, P. B., 1969: Slow oscillations in an ocean of varying depth. Part 2. Islands and seamounts. *J. Fluid Mech.*, **37**, 191–205.

Rippeth, T. P., E. Williams, and J. H. Simpson, 2002: Reynolds stress and turbulent energy production in a tidal channel. *J. Phys. Oceanogr.*, **32 (4)**, 1242–1251.

Sanson, L. Z., 2010: Solutions of barotropic trapped waves around seamounts. *J. Fluid Mech.*, **661**, 32–44.

Sciremammano, F., 1980: The nature of the poleward heat-flux due to low-frequency current fluctuations in Drake Passage. *J. Phys. Oceanogr.*, **10 (6)**, 843–852.

Sherman, J. T. and R. Pinkel, 1991: Estimates of the vertical wave-number frequency-spectra of vertical shear and strain. *J. Phys. Oceanogr.*, **21 (2)**, 292–303.

Shroyer, E. L., J. N. Moum, and J. D. Nash, 2010: Vertical heat flux and lateral mass transport in nonlinear internal waves. *Geophys. Res. Lett.*, **37**, L08 601.

Sloyan, B. M., 2005: Spatial variability of mixing in the Southern Ocean. *Geophys. Res. Lett.*, **32 (18)**, L18 603.

Smith, I. J., D. P. Stevens, K. J. Heywood, and M. P. Meredith, 2010: The flow of the Antarctic Circumpolar Current over the North Scotia Ridge. *Deep-Sea Res.*, **57**, 14–28.

Smith, W. H. F. and D. T. Sandwell, 1997: Global sea floor topography from satellite altimetry and ship depth soundings. *Science*, **277 (5334)**, 1956–1962.

St Laurent, L. and C. Garrett, 2002: The role of internal tides in mixing the deep ocean. *J. Phys. Oceanogr.*, **32 (10)**, 2882–2899.

Thomson, D. J., 1982: Spectrum estimation and harmonic-analysis. *J. Proc. IEEE*, **70 (9)**, 1055–1096.

Thorpe, S. A., 1992: The generation of internal waves by flow over the rough topography of a continental slope. *Proc. Roy. Soc. London*, **439 (1905)**, 115–130.

Thorpe, S. A., 2005: *The Turbulent Ocean*. Cambridge University Press.

Toole, J. M., K. L. Polzin, and R. W. Schmitt, 1994: Estimates of diapycnal mixing in the abyssal ocean. *Science*, **264 (5162)**, 1120–1123.

Walkden, G. J., K. J. Heywood, and D. P. Stevens, 2008: Eddy heat fluxes from direct current measurements of the Antarctic Polar Front in Shag Rocks Passage. *Geophys. Res. Lett.*, **35 (6)**, L06 602.

Wunsch, C. and R. Ferrari, 2004: Vertical mixing, energy and the general circulation of the oceans. *Annu. Rev. Fluid Mech.*, **36**, 281–314.

List of Tables

TABLE 1. Instruments moored in Shag Rocks Passage from 06/05/03 - 27/11/04. mab = metres above bottom.

Mooring	Latitude	Longitude	Water Depth	Instrument Type	mab	Sampling Interval
Shag 1a	53°18.251′S	48°54.828′W	2960 m	Aanderaa RCM8	30	hourly
Shag 1b	53°09.018′S	48°29.948′W	2766 m	Aanderaa RCM8	400	hourly
				RDI 300 kHz Workhorse ADCP	600	20 mins
				Pressure/Temp. logger XR420 TD	600	3 mins
Shag 2a	53°02.510′S	48°02.313′W	2996 m	Aanderaa RCM8	30	hourly
				Aanderaa RCM8	100	hourly
Shag 2b	53°02.510′S	48°02.770′W	2999 m	Aanderaa RCM8	400	hourly
				RDI 75 kHz LongRanger ADCP	600	2-hourly
				Pressure/Temp. logger SBE 39	600	10 mins
Shag 3a	52°55.653′S	47°45.992′W	2928 m	Aanderaa RCM8	30	hourly
				Aanderaa RCM8	100	hourly
Shag 3b	52°55.670′S	47°45.550′W	2945 m	Aanderaa RCM8	400	hourly
				RDI 300 kHz Workhorse ADCP	600	20 mins

Table 2. Various statistics of the time series of integrated shear variance (ISV), buoyancy frequency ($\overline{N}$), dissipation rate (ϵ), diffusivity (κ_z) and rotary coefficient (R.C.), with the equivalent values as found by the LADCP, taken from the nearest station of the deployment cruise and averaged over the same depths observed by the moored ADCP. (st. dev. = standard deviation, %ile = percentile. All values given to 2 s.f., except for the buoyancy frequency which is given to 2 d.p. in order to distinguish the median, 75th percentile, maximum and mean. All time series values are after applying the running 24-hour mean. The skewness and excess kurtosis are not scaled by the factors given in the column headings, and are both dimensionless numbers.)

	ISV $\times 10^{-7}\,\mathrm{s}^{-2}$	$\overline{N}$ $\times 10^{-3}\,\mathrm{s}^{-1}$	ϵ $\times 10^{-9}\,\mathrm{W\,kg}^{-1}$	κ_z $\times 10^{-4}\,\mathrm{m}^2\,\mathrm{s}^{-1}$	R.C.
minimum	2.7	0.57	0.32	0.54	-0.68
25th %ile	5.3	1.01	1.3	2.2	-0.22
median	6.2	1.05	1.8	3.3	-0.093
75th %ile	7.6	1.09	2.6	4.9	0.029
maximum	24	1.11	28	57	0.51
mean	6.6	1.05	2.2	4.1	-0.10
st. dev.	2.1	0.06	1.7	3.4	0.19
skewness	1.6	-1.62	4.4	4.8	-0.19
excess kurtosis	6.0	7.68	42	51	-0.066
1st value	8.4	0.93	3.1	7.2	-0.070
LADCP	5.1	0.90	1.9	6.4	-0.23

TABLE 3. Correlations between the time series of temperature (T) 600 mab, buoyancy frequency, integrated shear variance, dissipation rate, rotary coefficient and diffusivity, all after applying the running 24-hour mean. Values in bold are significant at the 95% confidence level.

	T	ISV	$\overline{N}$	ϵ	R.C.	κ_z
T	1	-0.19	**0.47**	-0.23	0.27	-0.26
ISV		1	-0.04	**0.94**	**-0.38**	**0.89**
$\overline{N}$			1	-0.15	0.15	**-0.31**
ϵ				1	**-0.39**	**0.98**
R.C.					1	**-0.40**
κ_z						1

List of Figures

5 Some example vertical wavenumber spectra. The thin solid lines are the spectra for the times when the calculated diffusivity was the minimum (pale grey), median (darker grey), and maximum (black) value of the time series. The thick solid black line is the GM model spectrum, the dotted line is the spectrum for shear noise of velocity variance (3.2 cm $s^{-1})^2$/nping, where nping is the number of pings used for each velocity measurement. The vertical dashed lines are the limits of integration, corresponding to wavelengths of 300 m and 90 m. 48

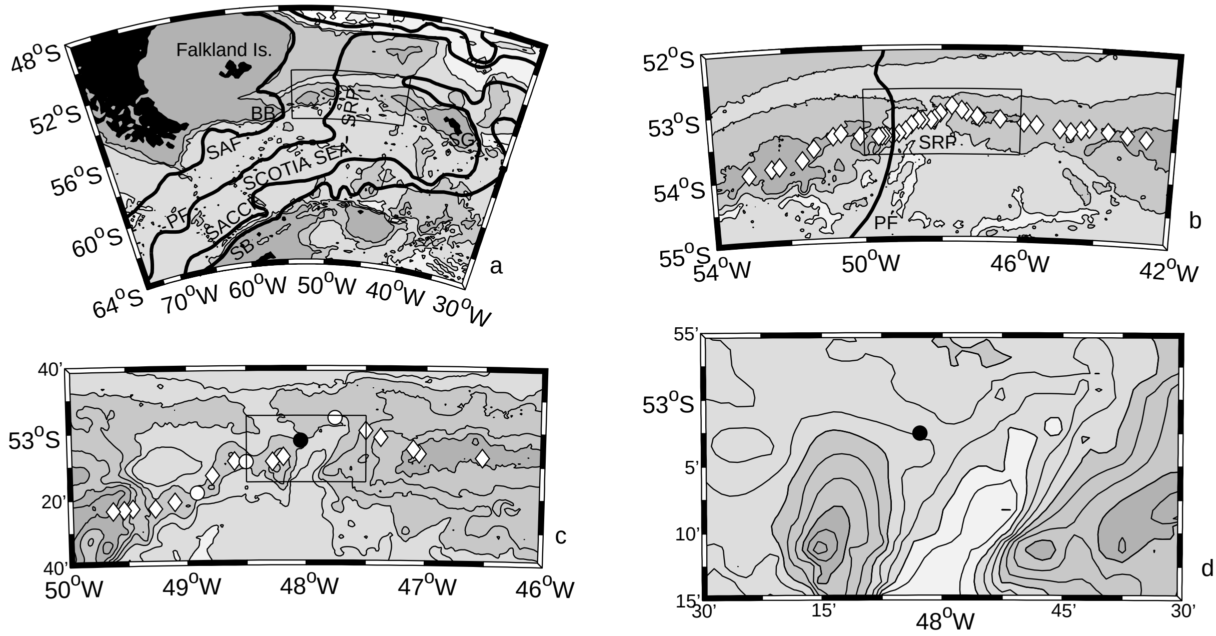

Fig. 1. Regional map, with bathymetry from Smith and Sandwell (1997), and climatological trajectories of the ACC fronts from Orsi et al. (1995). (SAF = Subantarctic Front, PF = Polar Front, SACCF = Southern ACC Front, SB = Southern Boundary of the ACC.) Contour intervals are every 1500m in (a) and (b). The following topographic features are indicated by their initials: Burdwood Bank (BB), South Georgia (SG), Shag Rocks Passage (SRP). (a) Overview of the Scotia Sea. (b) North Scotia Ridge, with deployment cruise station locations indicated by diamonds. (c) Overview of Shag Rocks Passage. Contour intervals are now every 500m with shading every 1500m. The circles are the mooring locations, at which CTDs were deployed during both the deployment and recovery cruises; other deployment cruise station locations are indicated by diamonds. From west to east, the moorings are Shag1a, Shag1b, Shag2(a and b) and Shag3(a and b). This study is concerned primarily with mooring Shag2b, which is the black circle. (d) Shag Rocks Passage. Contour intervals are now every 200m with shading every 600m. The black circle is mooring Shag2b. Note the seamount of height $\sim$ 1600 m southeast of the mooring location. In (a), (b) and (c), the thin black rectangle indicates the area shown in the next panel.

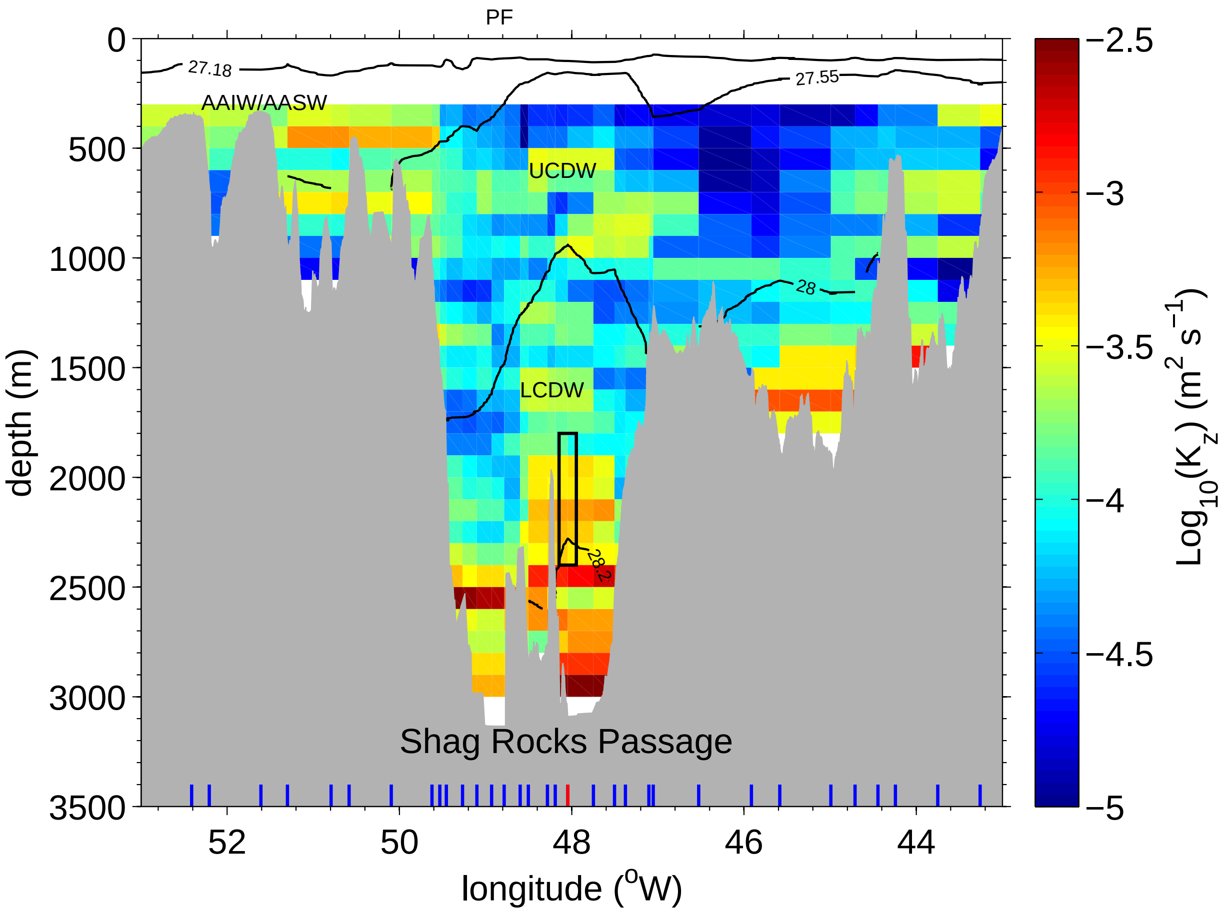

FIG. 2. Vertical diffusivity (κ_z) along the North Scotia Ridge. Density surfaces, shown as black lines, separate different water masses (AAIW/AASW, Antarctic Intermediate Water/Antarctic Surface Water, $27.18 < \gamma^n < 27.55$; UCDW, Upper Circumpolar Deep Water, $27.55 < \gamma^n < 28.00$; LCDW, Lower Circumpolar Deep Water, $28.00 < \gamma^n < 28.20$, where γ^n is the neutral density, in kg m^{-3}, as defined by Jackett and McDougall 1997). Station positions are indicated by blue tickmarks at the base of the topography, with the mooring position as a red tickmark. The approximate location of the Polar Front is marked as PF on the upper axis. The black rectangle in Shag Rocks Passage gives an approximate indication of the extent of the LongRanger ADCP at mooring Shag 2b; the horizontal extent of the rectangle is for illustrative purposes only.

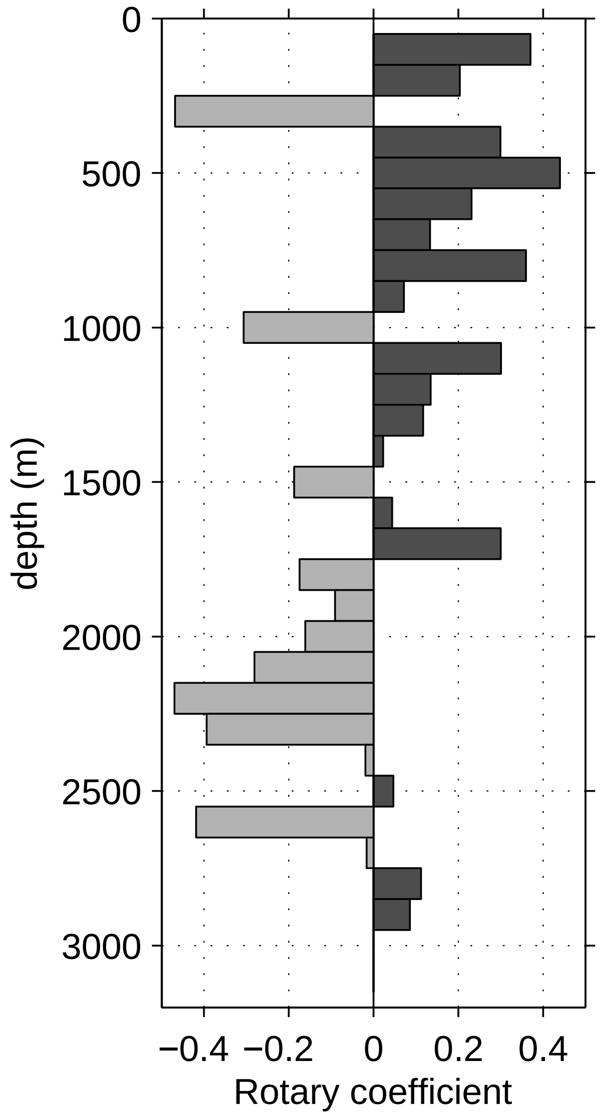

FIG. 3. Rotary coefficient (dimensionless) for the stations in Shag Rocks Passage deeper than 2000 m. Values less than zero indicate upward propagation of energy, values greater than zero indicate downward propagation.

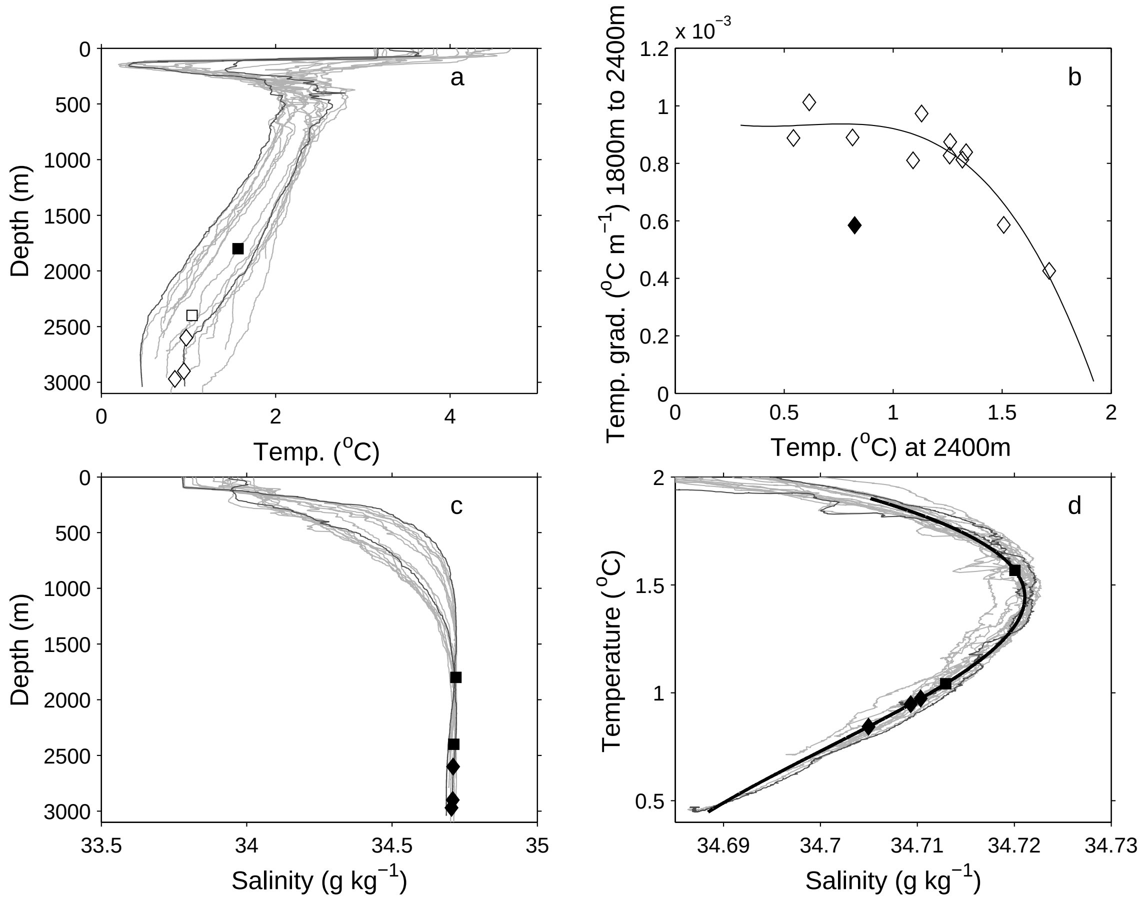

FIG. 4. The extrapolation of temperature and fitting for salinity used to derive the timeseries of buoyancy frequency. In (a), (c) and (d), the grey lines are profiles of the Shag Rocks Passage CTD stations, with the darker grey being the closest station of each cruise. (a) Temperature against depth. The white diamonds are the mean temperatures recorded by the three RCMs, 30, 100 and 400 meters above bottom (mab), the white square is the mean temperature recorded by the sensor on the ADCP 600 mab, and the black square is the mean extrapolated temperature at 1200 mab. (b) Relationship between the temperature at 2400 m and the temperature gradient between 1800 and 2400 m, i.e., the depth range observed by the moored ADCP. The black line is the cubic fit used to extrapolate temperatures above 2400m during the mooring time series. The black diamond is station 58 of the deployment cruise, which was excluded as an outlier. (c) Salinity against depth. The black diamonds and squares are the mean fitted salinities at 30, 100, 400, 600 and 1200 mab. (d) T–S relationship. The black line represents the cubic fit used to calculate salinity from temperature, and the black diamonds and squares represent the mean T–S values at 30, 100, 400, 600 and 1200 mab.

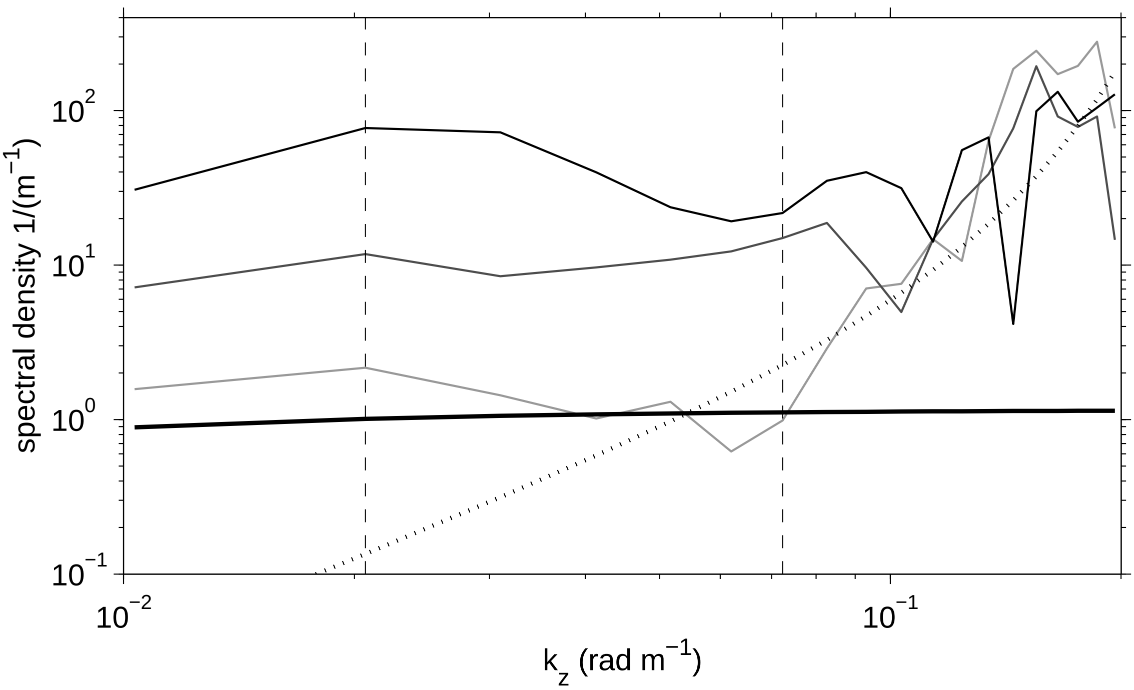

FIG. 5. Some example vertical wavenumber spectra. The thin solid lines are the spectra for the times when the calculated diffusivity was the minimum (pale grey), median (darker grey), and maximum (black) value of the time series. The thick solid black line is the GM model spectrum, the dotted line is the spectrum for shear noise of velocity variance $(3.2 \text{ cm s}^{-1})^2$/nping, where nping is the number of pings used for each velocity measurement. The vertical dashed lines are the limits of integration, corresponding to wavelengths of 300 m and 90 m.

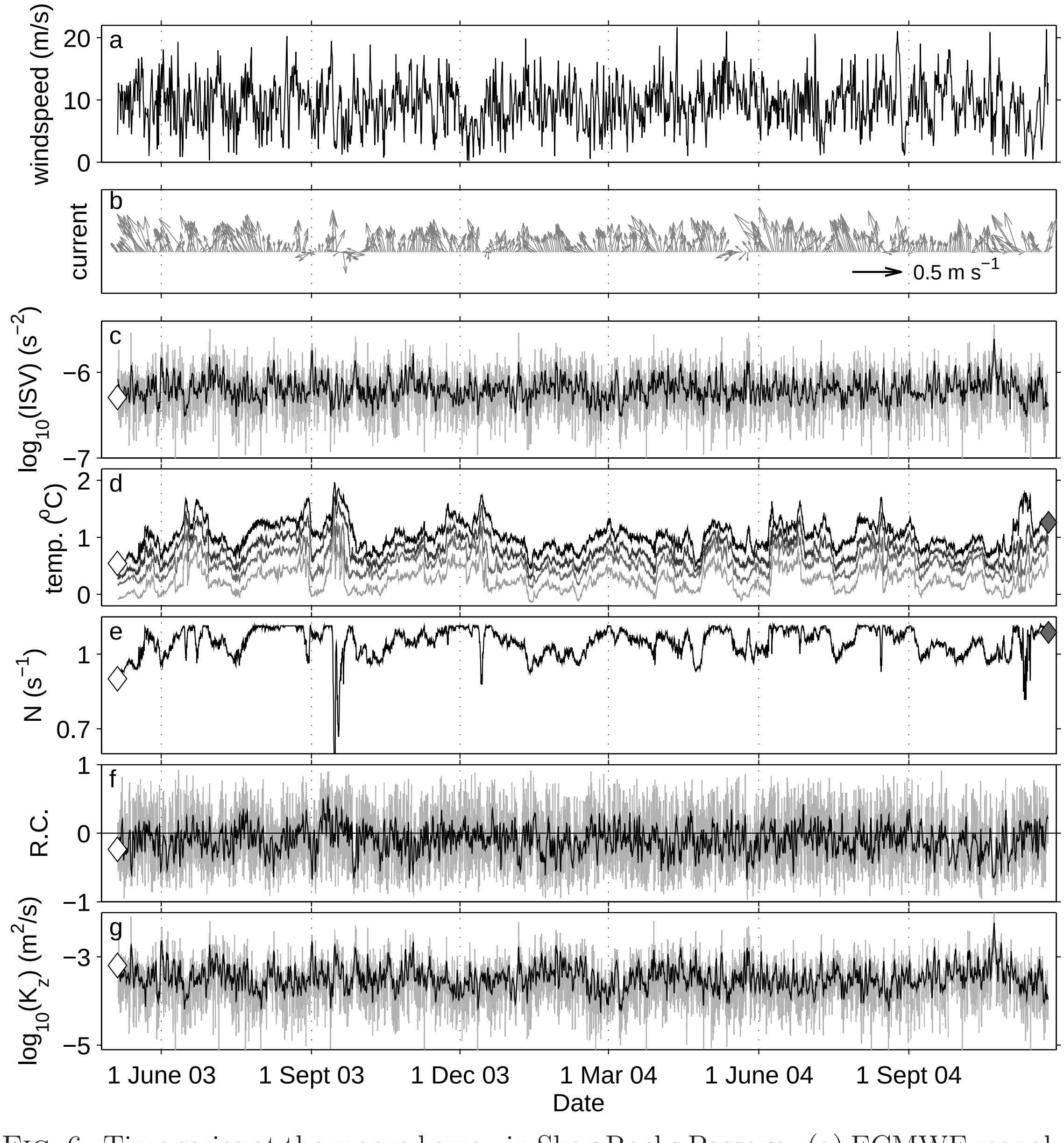

FIG. 6. Time series at the moored array in Shag Rocks Passage. (a) ECMWF reanalysis wind speed from the closest grid point. (b) Depth-averaged daily currents recorded by the moored ADCP. The first arrow at the start of the time series is that recorded by the LADCP on the closest station of the deployment cruise (station 56). (c) Log_{10}(integrated shear variance) (s^{-2}). (d) Temperatures (°C). The palest line is the temperature recorded 30 mab, offset by -0.6°C, the mid-grey line is that recorded 100 mab, offset by -0.4°C, the darkest grey line is that recorded 400 mab, offset by -0.2°C, and the black line is that recorded 600 mab. The white diamond is that recorded by the CTD at station 56, and the grey diamond is that recorded by the CTD on the closest station of the recovery cruise (station 19), both at 2400 m. (e) Buoyancy frequency ($\times 10^{-3}$ s^{-1}). The grey diamond is that recorded at station 19 of the recovery cruise, averaged over the depths observed by the moored ADCP. (f) Rotary coefficient (dimensionless). (g) $\text{Log}_{10}(\kappa_z)$ (m^2 s^{-1}). The horizontal line is the median value. For subplots (c),(e),(f) and (g), the grey line is the unsmoothed quantities, the black line is daily average values, and the white diamond is that recorded at station 56 of the deployment cruise, averaged over the depths observed by the moored ADCP.

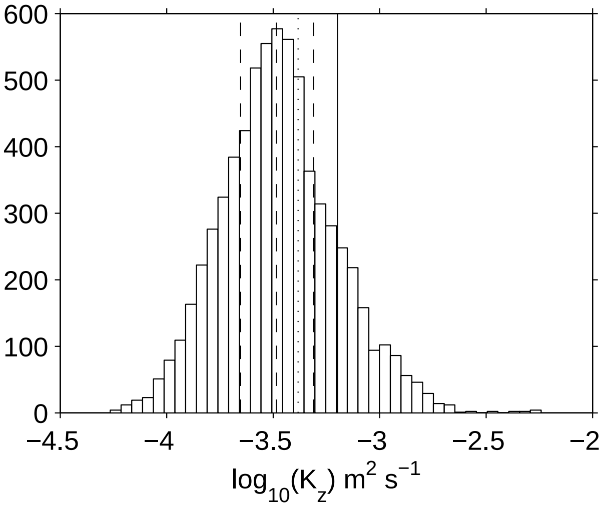

Fig. 7. Distribution of time series diffusivity. The dashed lines are the 25th, 50th (median) and 75th percentiles, the dotted line is the mean, and the solid line is the diffusivity found by the LADCP, averaged over the waterdepth observed by the moored ADCP.

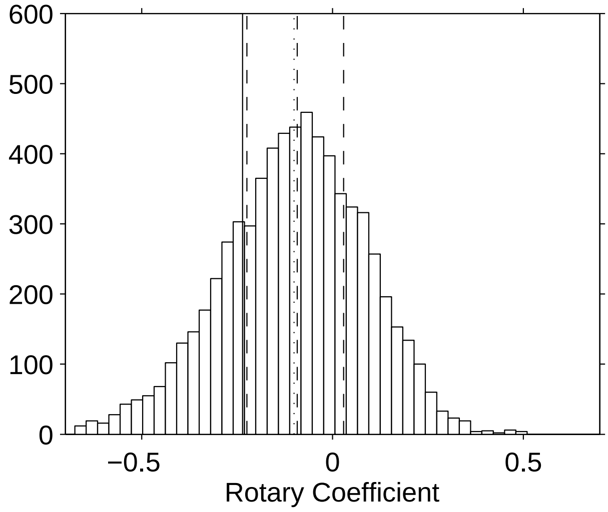

Fig. 8. Distribution of time series rotary coefficient. The dashed lines are the 25th, 50th (median) and 75th percentiles, the dotted line is the mean, and the solid line is the rotary coefficient found by the LADCP, averaged over the waterdepth observed by the moored ADCP.

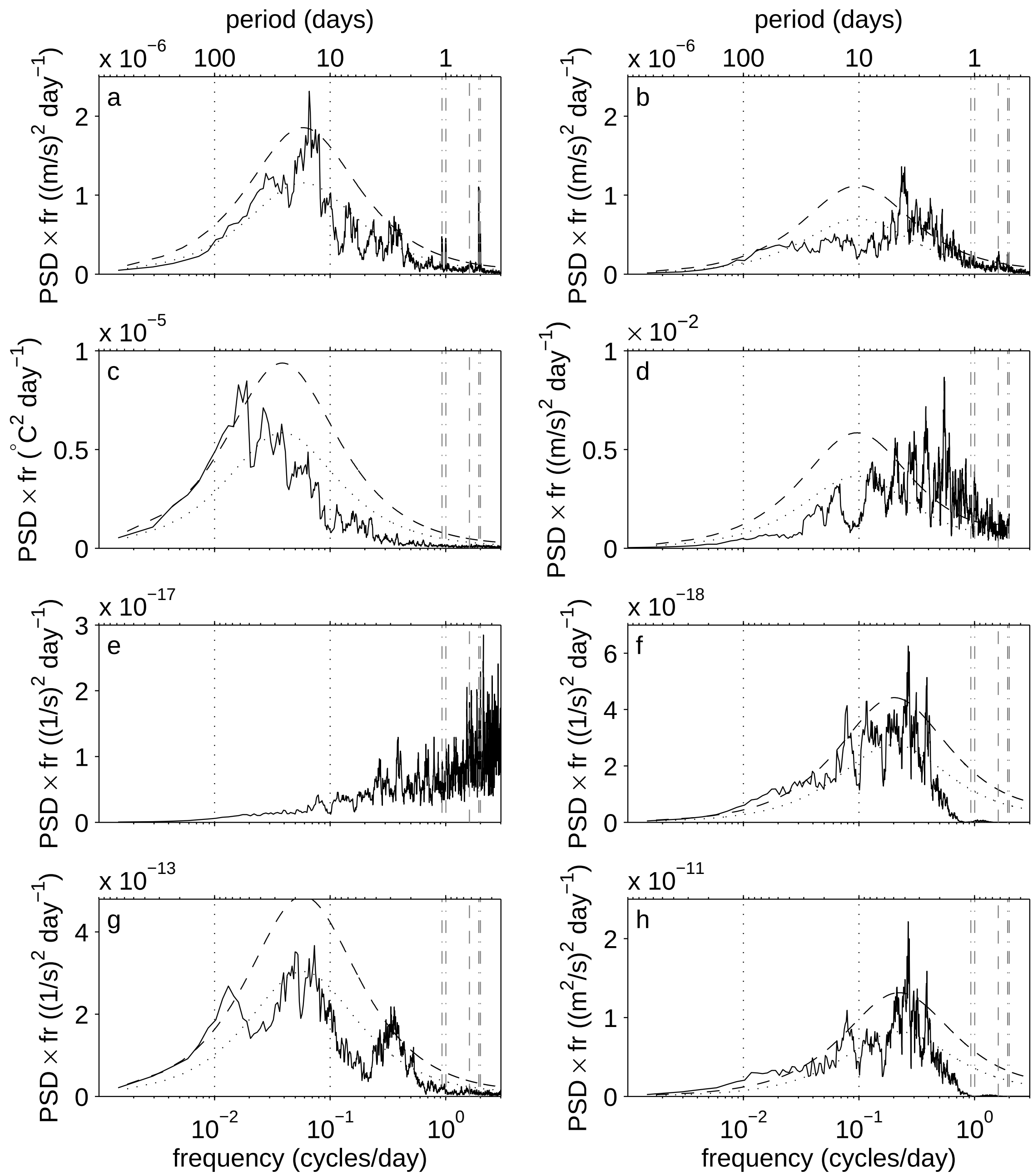

FIG. 9. Variance preserving spectra. In each plot, the vertical axis is the power spectral density × frequency (PSD × fr). The dotted curve is the theoretical red noise spectrum based on the lag-1 auto-correlation coefficient, and the dashed curve is the 95% confidence limit. The vertical dashed line is the inertial frequency, and the vertical dot-dash lines are the main diurnal and semi-diurnal tidal frequencies. (These are O1, K1, M2 and S2 from left to right, although M2 and S2 are very close together and so may appear as one thick dot-dash line.) (a) Northward and (b) eastward depth-mean velocity: these are largely representative of the spectra for individual levels as the currents in this area are quite barotropic. (c) Temperature from the instrument located 600 mab. (d) 6-hourly ECMWF reanalysis wind speed at the nearest grid point to mooring Shag2b. (e) Integrated shear variance without the smoothing described in section 3.a.iv. (f) Integrated shear variance with the smoothing described in section 3.a.iv. (g) Buoyancy frequency. (h) κ_z with the smoothing described in section 3.a.iv.

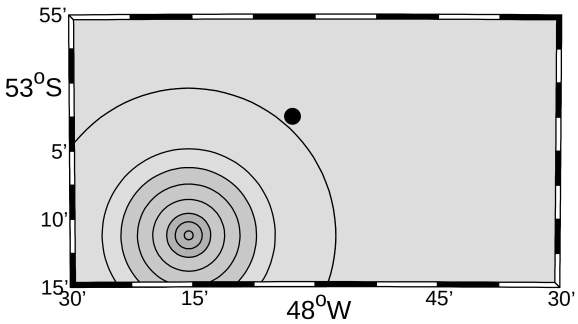

FIG. 10. Idealised axisymmetric seamount used with the Brink model, for comparison with Fig. 1d. Contour intervals are every 200m with shading every 600m in the same colors as Fig. 1d. The black circle is mooring Shag2b.